JGR Atmospheres

RESEARCH ARTICLE
10.1029/2018JD029809

Optical Properties and Radiative Forcing of Aged BC due to Hygroscopic Growth: Effects of the Aggregate Structure

Chen Zeng[1,2], Chao Liu[1,2], Jiangnan Li[3], Bin Zhu[1,2], Yan Yin[1,2], and Yuan Wang[4]

[1]Collaborative Innovation Center on Forecast and Evaluation of Meteorological Disasters, Nanjing University of Information Science and Technology, Nanjing, China, [2]Key Laboratory for Aerosol-Cloud-Precipitation of China Meteorological Administration, School of Atmospheric Physics, Nanjing University of Information Science and Technology, Nanjing, China, [3]Canadian Centre for Climate Modelling and Analysis, Science and Technology Branch, Environment Canada, University of Victoria, Victoria, British Columbia, Canada, [4]Division of Geological and Planetary Science, California Institute of Technology, Pasadena, CA, USA

Key Points:
- Aggregate geometry affects both the optical properties and radiative forcing of aged BC during hygroscopic growth
- Hygroscopic growth enhances aged BC scattering more significantly than absorption, offsetting the BC warming effect at the TOA
- A model based on a core-shell structure reasonably estimates the forcing at the TOA but differs in the forcing at the SFC and ATMOS

Correspondence to:
C. Liu,
chao_liu@nuist.edu.cn

Citation:
Zeng, C., Liu, C., Li, J., Zhu, B., Yin, Y., & Wang, Y. (2019). Optical properties and radiative forcing of aged BC due to hygroscopic growth: Effects of the aggregate structure. *Journal of Geophysical Research: Atmospheres*, *124*, 4620–4633. https://doi.org/10.1029/2018JD029809

Received 13 OCT 2018
Accepted 25 MAR 2019
Accepted article online 2 APR 2019
Published online 17 APR 2019

Abstract Black carbon (BC) particles become hydrophilic after mixing with soluble matter in the atmosphere, and their optical and radiative properties can be significantly modified accordingly. This study investigates the impact of aggregate structure on optical and radiative properties of aged BC, that is, BC coated by sulfate or organic aerosols, especially during hygroscopic growth. A more realistic BC morphology based on fractal aggregates is considered, and inhomogeneous mixtures of BC aggregates are treated more realistically (with respect to particle geometries) in the multiple sphere T-matrix method for optical property simulations. As relative humidity increases, BC extinction is significantly enhanced due to an increase in scattering, and the enhancement depends on the amount and hydrophilicity of the coating. The absorption exhibits less variation during hygroscopic growth because the coating of aerosols already leads to BC absorption close to the maximum. Furthermore, hygroscopic growth not only results in negative radiative forcing (RF) at the top of the atmosphere but also slightly weakens the absorption in the atmosphere (inducing a negative RF in the atmosphere). Compared to the more realistic model with BC as aggregates, the currently popular core-shell model reasonably approximates the top of the atmosphere RF but underestimates the atmospheric RF due to hygroscopic growth by up to 40%. Furthermore, for the RF caused by internal mixing, the core-shell model overestimates the RFs at the surface and in the atmosphere by ~10%.

1. Introduction

Aerosols affect the Earth's weather and climate directly through the radiative transfer process in the atmosphere (Wang et al., 2015). Among different types of aerosols, black carbon (BC), a product of incomplete combustion from coal, diesel engines, biofuels, and biomass burning, contributes a significant positive component of aerosol radiative forcing (RF; Hansen et al., 1997; Jacobson, 2001; Menon et al., 2002). Although BC has a relatively small mass concentration compared to other aerosols (e.g., a global mean columnar burden of ~0.14 mg/m^2; Myhre et al., 2013), it serves as the second strongest anthropogenic global warming agent, only after carbon dioxide (Bond et al., 2013; Ramanathan & Carmichael, 2008). Specifically, BC warms the atmosphere by absorbing solar radiation and produces significant positive RF at the top of the atmosphere (TOA) and negative RF at the surface (SFC; Ramanathan & Carmichael, 2008). The globally averaged BC direct RF at the TOA and in the atmosphere (ATMOS) can reach up to 1.1 W/m^2 (with 90% uncertainty limits from 0.17 to 2.1 W/m^2) and 2.75 W/m^2, respectively (Bond et al., 2013), whereas and regional BC RF may reach as large as 7 W/m^2 or even 10 W/m^2 at the TOA (Chung, Lee, et al., 2012; K. Li et al., 2016).

After being emitted into the atmosphere, BC particles become aged and mixed with other aerosols, known as the "aging" process (Weingartner et al., 1997). The aging process can happen in a few minutes to days (He et al., 2016; Riemer et al., 2010) and can be faster in a polluted atmosphere (Peng et al., 2016; Wang et al., 2018). Once mixed with other aerosols, such as sulfate, nitrate, and organics, the optical properties and RF of the BC particles can be substantially changed. The effects of nonabsorbing coatings on the optical and radiative properties of complex BC aggregates have been extensively studied (Chung, Ramanathan,

et al., 2012; Liu et al., 2017). Most numerical studies as well as some observations have indicated that the absorption of BC may be enhanced after being coated by even nonabsorbing materials (Schnaiter et al., 2005; Wang et al., 2013), which may lead to a positive RF compared with the externally mixed conditions (Srivastava & Ramachandran, 2013), whereas some field observations show relatively weak absorption enhancement (Cappa et al., 2012). Moreover, the coating also increases scattering due to the enlarged particle size, and the nonabsorbing aerosol components themselves produce a negative RF at the TOA. As a result, internal mixing of BC and other aerosols may not necessarily increase BC RF (Lesins et al., 2002).

From the microphysical point of view, BC and nonabsorbing aerosols also exhibit different behaviors in the humid atmosphere. Bare BC is hydrophobic, whereas soluble inorganics (e.g., sulfate and nitrate; Hämeri et al., 2000) and organic carbon (OC) are hydrophilic and can uptake moisture to different degrees. Consequently, aged BC (i.e., BC with sulfate, nitrate, or OC coating) also uptakes moisture in the atmosphere and experiences hygroscopic growth due to the coating component (He et al., 2015). Complex aerosol formation, mixing, and hygroscopic growth processes are fundamental to air pollution, radiative transfer, and cloud formation and have been extensively studied by state-of-the-art atmospheric chemistry/aerosol models, for example, GOCART, MADE, MOSAIC, and TOMAS (Ackermann et al., 1998; Adams & Seinfeld, 2002; Aquila et al., 2011; Chin et al., 2000; Ching et al., 2016; Fierce et al., 2016, 2017; Lee & Adams, 2010; Matsui et al., 2013; Riemer et al., 2009; Zaveri et al., 2008). These models mainly focus on and differ in aerosol mixing compositions and sizes, and the optical and radiative properties are not discussed in detail. For example, these models normally treat the mixtures of BC and other aerosol components as homogeneous spheres or core-shell spheres (BC as the spherical core), and the corresponding optical properties can be obtained by the classic Mie theory. However, BC particles normally occur in the form of nonspherical aggregates in the atmosphere, and a spherical assumption may introduce significant errors in estimating BC optical properties (J. Li et al., 2016).

In addition to the complex mixing and hygroscopic growth process, realistic BC morphology has been extensively considered for BC optical properties (Adler et al., 2010; Kahnert et al., 2012; Kahnert & Devasthale, 2011; Sorensen, 2001). However, the two factors (aggregate structure and hygroscopic growth) are seldom combined for optical and RF estimations, and how the BC aggregate structure influences its optical and radiative properties during hygroscopic growth is still unclear. Therefore, this study aims to account for the aggregate structure effects of aged BC during hygroscopic growth, with a focus on optical aspects. This paper is organized as follows. The numerical models for the microphysical, optical, and radiative properties of aged BC during hygroscopic growth are introduced in section 2. The influences of aggregate structures on the optical properties and RF during hygroscopic growth are discussed in section 3. Finally, the conclusions of this work are presented in section 4.

2. Methodologies

2.1. Microphysical Properties

Microscopic images show that BC particles exist in the form of clusters containing hundreds or even thousands of spherical monomers, which are in the range of 20–60 nm in diameter (Chakrabarty et al., 2006; Wang et al., 2017). These BC aggregates can be specified mathematically as fractal aggregates and follow the statistic scaling rule (Sorensen, 2001):

$$N = k_{\mathrm{f}}\left(\frac{R_{\mathrm{g}}}{a}\right)^{D_{\mathrm{f}}}, \tag{1}$$

with $R_{\mathrm{g}}^2 = \frac{1}{N}\sum_{n=1}^{N}\left(\overrightarrow{r_n}-\overrightarrow{r_0}\right)^2$. Here N is the number of monomers in the aggregate, and a is the monomer radius. k_{f} and D_{f} are the fractal prefactor and fractal dimension, respectively, and describe the overall structure of the aggregates. $\overrightarrow{r_n}$ and $\overrightarrow{r_0}$ denote the position vectors of the center of each monomer and aggregate mass center, respectively. Compact aggregates require larger fractal parameters (k_{f} or D_{f}) to follow equation (1). After emission, "fresh" BC particles exhibit lacy chain-like structures with relatively small D_{f} (Smith & Grainger, 2014). Then, during the so-called aging process, the structure and chemical composition of BC particles may be significantly changed, and these BC particles become compact aggregates (e.g., Figures 1a and 1b). Thus, this study treats BC geometries as fractal aggregates similar to the actual ones in the atmosphere. Figure 1f shows an example of a modeled fractal aggregate that closely represents the

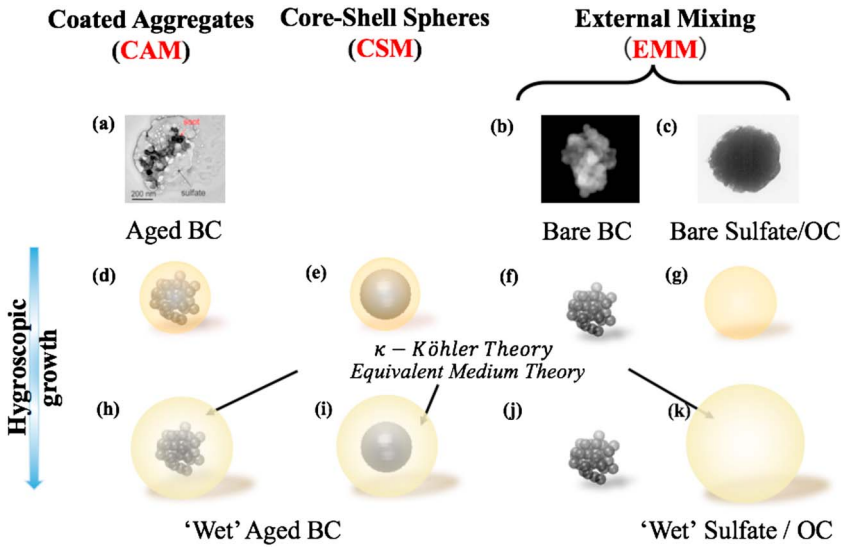

Figure 1. Description of BC aging and hygroscopic growth processes, including external and internal mixing geometries. The BC particles are considered to have fractal aggregate geometries, and the κ-Köhler and equivalent medium theories are combined to quantify the influences of hygroscopic growth on particle microphysical properties. (a) An aged BC image; (b) a bare BC image; (c) a bare OC image; (d) a coated-aggregate BC particle before hygroscopic growth; (e) a core-shell sphere before hygroscopic growth; (f) a BC aggregate; (g) a sulfate/OC sphere; (h) a coated-aggregate BC particle after hygroscopic growth; (i) a core-shell sphere after hygroscopic growth; (j) a BC aggregate; and (k) a sulfate/OC sphere after hygroscopic growth. BC = black carbon; OC = organic carbon.

realistic BC particles in Figure 1b. The aggregates are numerically generated by a tunable aggregation algorithm (Filippov et al., 2000), and we use the fractal parameters of $k_f = 1.2$ and $D_f = 2.8$ to represent these aged BC particles with relatively compact structures (Liu et al., 2017; Sorensen, 2001).

In the ambient atmosphere, BC aggregates can be easily attached to or coated by aerosols such as sulfate and OC, and show structures similar to those in Figure 1a (Wang et al., 2017). Thus, we consider spherical coatings in this study, and the "aged/mixed BC" particles are treated as a large coating sphere and small spherical BC monomers, as shown in Figure 1d. The BC aggregates can be partially or entirely embedded in the spherical coating depending on the coating amount and relative positions of the two components, and such geometries are similar to those observed in the atmosphere (Adachi et al., 2010; Liu et al., 2015). For the coated BC aggregates, the aggregate mass center and the coating sphere center are assumed to be coincident, and the effects of the BC core placement with respect to the coating center on the optical properties are briefly discussed. Similar aggregate-based morphologies have been developed in the past for optical property investigations (Adler et al., 2010; Kahnert et al., 2012; Liu & Mishchenko, 2018), whereas the hygroscopic process and RF have not been considered in these studies. For simplification, we assume that the mixed material, that is, the coating, is homogeneous (either sulfate or OC), and more realistic cases with different coating materials may be considered by coupling our model with more sophisticated aerosol chemistry models (Fierce et al., 2016, 2017; Matsui et al., 2018). Nitrate has a refractive index and hygroscopicity similar to those of sulfate and is expected to lead to similar effects.

Another important factor that should be carefully defined is the coating fraction, that is, the fractions of coating components for different-sized BC particles. Recent numerical models have considered particle-resolved mixing compositions, and the results show that models based on a constant BC fraction may yield significant errors in aerosol absorption and optical properties (Fierce et al., 2016; Matsui et al., 2018; Zaveri et al., 2010). More realistic coating fraction variation, particularly the coating fraction as a function of BC size, should be considered. In a chamber experiment carried out by Schnaiter et al. (2005), diesel soot particles were coated by secondary organic compounds produced by in situ ozonolysis of α-pinene for 24 hr, and size distributions before and after the aging procedure were obtained. By a few simple assumptions, C. Liu et al. (2018) derived a relationship between the equivalent-volume radii of BC before and after coating and further obtained an "observation-based" coating fraction variation. We use their relationship to define our mixed BC, and

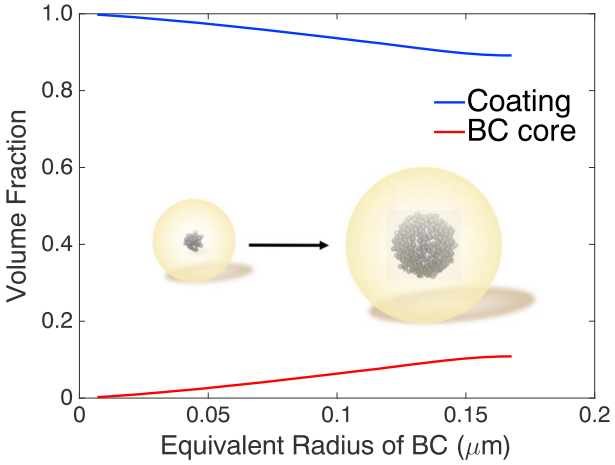

Figure 2. Volume fractions of BC and coating material in the mixed BC as a function of BC equivalent-volume radius. The relationship is derived from observations by Schnaiter et al. (2005), and more details about the derivation can be found in C. Liu et al. (2018). BC = black carbon.

Figure 2 illustrates the BC volume fraction as a function of BC core size. The BC volume fraction increases from under 1% to slightly over 10% as the BC size increases, which corresponds to a relatively heavy coating scenario. The trend agrees with the modeling results from Fierce et al. (2016). As a result, we adopt this observation-based relationship to define internally mixed BC particles. Note that in the real atmosphere, aged BC particles can have extremely complex and different shapes and coating amounts (Liu et al., 2017), and we focus on only the model described above to investigate the effects of the BC aggregate structure.

Aerosols such as sulfate, nitrate, and OC are hydrophilic and grow by absorbing water vapor after the surrounding relative humidity (RH) reaches its critical point. As illustrated in Figure 1, "bare sulfate" may change from the small sphere in Figure 1g to the larger sphere in Figure 1k, and the change in colors indicates the change in overall particle material from pure sulfate to a homogeneous mixture of sulfate and water. In such a hygroscopic growth process, the particle size may grow exponentially as RH increases. Meanwhile, aged BC with a hydrophilic coating also undergoes such hygroscopic growth in a humid environment due to the hydrophilic portion of the mixtures. The growth of homogeneous hydrophilic aerosols and coated BC particles can be quantified by the κ-Köhler theory (Chang et al., 2010; Cruz & Pandis, 2000), a relationship to estimate the change in size of aerosol particles due to condensation:

$$RH = \frac{(D/D_i)^3 - 1}{(D/D_i)^3 - (1-\kappa)} \exp\left(\frac{4\sigma M_w}{\rho_w RTD}\right), \tag{2}$$

where RH is the relative humidity, D_i and D are the diameters of aerosol droplets before and after hygroscopic growth, respectively. σ is the droplet surface tension. M_w and ρ_w are the molecular weight and density of water, respectively. R is the universal gas constant, and T is the temperature. κ is the hygroscopic parameter depending on aerosol compounds. The κ of a mixed particle is the volume-weighted average of the κ values of all components, and the κ values of sulfate, OC, and BC are 0.52, 0.14, and 0, respectively (H. Liu, Zhao, et al., 2014). For a particle with a given dry diameter D_i, its wet counterpart D can be easily determined by equation (2). Note that the κ-Köhler theory assumes that particles are spherical, so the impacts of aggregate geometry cannot be accounted for by hygroscopic growth. However, with the heavy spherical coating, aged BC particles have an overall spherical geometry, regardless of how significant the effects are.

The left panel of Figure 3 illustrates the influence of hygroscopic growth on the mixed BC radii, and the radii of aged BC with sulfate and OC coating before and after growth are shown. Because OC is less hydrophilic than sulfate, BC with OC coating becomes smaller than BC with sulfate coating under humid conditions, for example, the sizes of sulfate-coated BC particles at RH = 60% are similar to OC-coated BC particle sizes at RH = 90%. The right panel of Figure 3 shows the changes in the average radii of bare and aged BC (with either sulfate or OC coating) due to hygroscopic growth. We assume that the BC equivalent-volume radii follow a lognormal size distribution with a geometric mean radius of 0.06 μm and a standard deviation of 1.5 (Chakrabarty et al., 2006; J. Li et al., 2016; Schnaiter et al., 2005). With the coating fraction given in Figure 2, the coated BC has an equivalent radius of almost 0.2 μm. At RH = 90%, the average radius of the mixed particles with sulfate coating becomes ~1.7 times that of the dry case, comparable to the results by D. Liu et al. (2013), and the OC-coated BC increases by almost 30% in size. With such significant variations in particle composition and volume, BC optical properties and RF are expected to vary accordingly.

BC cannot form a solution with other aerosols or water, and the "wet aged BC" particles are inhomogeneous, containing a BC component and a sulfate/OC solution component. Additionally, the refractive indexes of the particles change due to the mixing of water and aerosols during hygroscopic growth. Sulfate/OC and uptaken water can form a homogeneous mixture with an effective refractive index determined by the

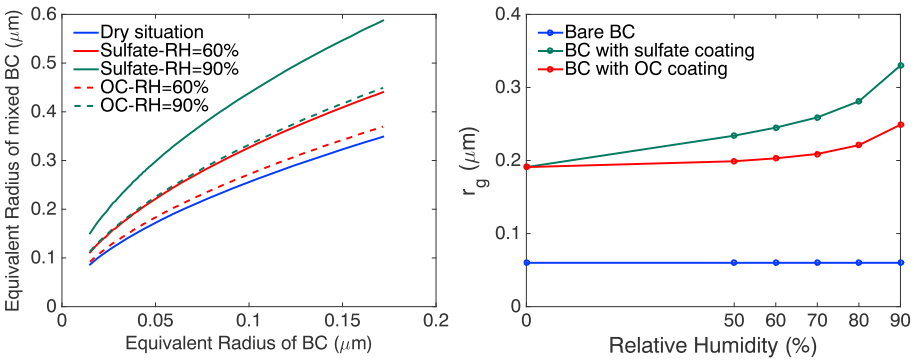

Figure 3. (left) Radii of BC mixtures with sulfate or OC coating before and after hygroscopic growth. (right) Radius variation in bare BC and internally mixed BC aerosols with sulfate and OC coatings during the hygroscopic growth process. The radius of BC in the dry situation is set to 0.06 μm, and the coating size of BC is determined by following the BC volume fraction given in Figure 2. BC = black carbon; OC = organic carbon; RH = relative humidity.

volume fractions of the two components. The effective refractive index of the sulfate/OC and water mixture can be obtained by various equivalent medium theories (EMTs; Chýlek et al., 2000). C. Liu, Panetta, et al. (2014) found that the simulations based on most EMTs lead to similar optical properties of mixed aerosol particles. The popular Bruggeman theory (C. Liu, Panetta, et al., 2014) used in this study is stated as follows:

$$f_s \frac{m_s^2 - m^2}{m_s^2 + 2m^2} + f_w \frac{m_w^2 - m^2}{m_w^2 + 2m^2} = 0. \tag{3}$$

Here m_s and m_w are the refractive indexes of sulfate and water, respectively, and f_s and f_w are their corresponding volume fractions ($f_s + f_w = 1$). m is the effective refractive index of the mixture. The refractive index of water is from Hale and Querry (1984), and the refractive indexes of sulfate, OC, and BC are obtained from Toon et al. (1976) and D'Almeida et al. (1991).

Figure 4 shows the refractive indexes of the aerosols and their mixtures before and after hygroscopic growth. The left panels are the wavelength-dependent refractive indexes of BC, sulfate, OC, and water. The real parts of the BC refractive indexes slightly increase with wavelength, while those of sulfate, OC, and water decrease with wavelength. The imaginary parts of refractive indexes represent aerosol absorptivity. BC and OC have imaginary parts on the order of 10^{-1} and 10^{-2}, while water and sulfate are almost nonabsorbing with values from less than 10^{-6} at visible wavelengths to approximately 10^{-3} at near-infrared wavelengths. In other words, both water and sulfate are almost nonabsorbing at visible wavelengths and become weakly absorbing in the near-infrared wavelengths. The middle and right panels of Figure 4 are refractive index variations at three wavelengths for sulfate and OC coating after absorbing water vapor at different ambient RHs. The refractive index of the mixture is calculated by the Bruggeman theory, that is, equation (3). With the increase in the water fraction due to the hygroscopic growth, the refractive index becomes close to that of water.

To summarize, mixed BC particles undergo complex physical and chemical processes and have complex mixing states (both composition and geometry) in a humid atmosphere, as briefly illustrated in Figure 1. Most importantly, a more realistic BC aggregate structure (i.e., the internal mixing case illustrated in Figures 1d and 1h) is considered in the whole process for optical simulations. We consider two other simplifications for comparison. First, the core-shell structure can be understood as a simplification of the internally mixed geometry of aged BC (i.e., replacing the BC aggregates by a single equivalent-volume sphere) and is widely used to approximate the influences of aging on BC optical properties and radiative effects at various scales (Ackermann et al., 1998; Adams & Seinfeld, 2002; Chin et al., 2000; Matsui et al., 2013; Zaveri et al., 2010). Thus, the core-shell model applied by these studies is considered for comparison. Second, the "external mixing" scenario considers BC and other aerosols independently. Compared to BC aggregates, sulfate or OC is geometrically more regular, and their overall geometries are treated simply as spheres in our modeling, that is, Figure 1g. The coated aggregate structure model is referred to as "CAM," and the core-shell model is shortened as "CSM." We also compare the results of external mixing as "EMM." The CSM can

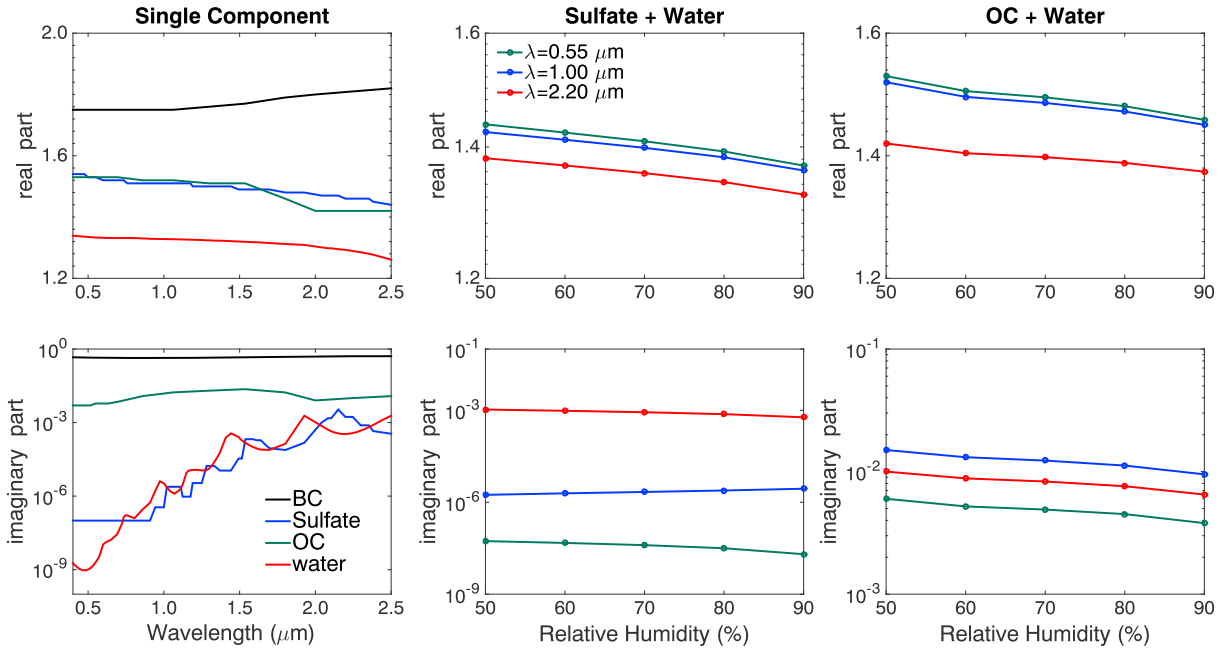

Figure 4. (left) Refractive indexes of bare BC, sulfate, OC, and water at different wavelengths. (middle and right) Effective refractive indexes of mixtures of sulfate and OC with water given by the Bruggeman theory (equation (4)). BC = black carbon; OC = organic carbon.

be simply understood as replacing the BC aggregate in the CAM by an equivalent-volume sphere. In the case of external mixing, the total sulfate amount is kept the same as that of the coating in the case of internal mixing, and the bare BC particles have no hygroscopic growth in the humid atmosphere.

2.2. Bulk Optical Properties

With the particle microphysical properties specially defined or given by aforementioned methods (e.g., size, shape, refractive index, and mixing states), it becomes straightforward to investigate their optical properties and radiative forcing. The state-of-art Multiple Sphere TMatrix (MSTM) method is adopted to calculate the single-scattering properties of the numerical particles with aggregate-based BC in Figure 1 (Mackowski & Mishchenko, 2011). Meanwhile, the optical properties of the CSM are given efficiently by the core-shell Mie theory.

All results discussed in this study are bulk optical properties averaged over an ensemble of different-sized particles, and lognormal distributions are used to represent aerosol size distributions. Again, the geometric mean radius and standard deviation of the BC equivalent-volume spheres are set as 0.06 μm and 1.5, respectively. The size distributions of the internally mixed particles (both before and after hygroscopic growth) are determined by conserving the bare BC amount and size distribution, and we assume that the BC particles and their size distribution are unchanged during the processes. For a fair comparison between the internal and external mixing conditions, the size distributions of sulfate and OC in the EMM case are given directly by the corresponding coating component in the CAM/CSM. In this way, the total volumes of the BC, sulfate, and OC components are conserved for all three cases. We assume that all particles are externally mixed in the EMM and that all particles are internally mixed in the CAM and CSM cases. The results of partially internal and partially external cases can be understood as weighted averages of the two extreme cases.

With the given particle size distribution, the bulk scattering properties for each aerosol, including extinction coefficient $\langle\sigma_{\mathrm{ext}}\rangle$, absorption coefficient $\langle\sigma_{\mathrm{abs}}\rangle$, single-scattering albedo $\langle\varpi\rangle$, and asymmetry factor $\langle g\rangle$, can be obtained (J. Li et al., 2016):

$$\langle\sigma_{\mathrm{ext}}\rangle = \int_{r_{\min}}^{r_{\max}} C_{\mathrm{ext}}(r)\cdot n(r)\mathrm{d}r, \tag{4}$$

$$\langle\sigma_{\mathrm{abs}}\rangle = \int_{r_{\min}}^{r_{\max}} C_{\mathrm{abs}}(r)\cdot n(r)\mathrm{d}r, \tag{5}$$

$$\langle \varpi \rangle = \frac{\int_{r_{\min}}^{r_{max}} C_{\text{ext}}(r)\cdot\varpi(r)\cdot n(r)\mathrm{d}r}{\int_{r_{\min}}^{r_{\max}} C_{\text{ext}}(r)\cdot n(r)\mathrm{d}r}, \tag{6}$$

$$\langle g \rangle = \frac{\int_{r_{\min}}^{r_{\max}} C_{\text{ext}}(r)\cdot\varpi(r)\cdot g(r)\cdot n(r)\mathrm{d}r}{\int_{r_{\min}}^{r_{\max}} C_{\text{ext}}(r)\cdot\varpi(r)\cdot n(r)\mathrm{d}r}. \tag{7}$$

$C_{\text{ext}}(r)$, $C_{\text{abs}}(r)$, $\varpi(r)$, and $g(r)$ are the extinction cross section, absorption cross section, single-scattering albedo, and asymmetry factor, at a single size r, and $n(r)$ is the lognormal size distribution of the BC equivalent-volume radii. BC equivalent radii up to 0.19 μm are considered for the integral. Equations (4)–(7) are used for homogeneous aerosols (sulfate, OC, and BC) or coated BC (CAM and CSM). For the EMM case, the bulk optical properties are given by

$$\langle \sigma_{\text{ext}} \rangle_{\text{EMM}} = \langle \sigma_{\text{ext}} \rangle_{\text{BC}} + \langle \sigma_{\text{ext}} \rangle_{\text{S}}, \tag{8}$$

$$\langle \sigma_{\text{abs}} \rangle_{\text{EMM}} = \langle \sigma_{\text{abs}} \rangle_{\text{BC}} + \langle \sigma_{\text{abs}} \rangle_{\text{S}}, \tag{9}$$

$$\langle \varpi \rangle_{\text{EMM}} = \frac{\langle \sigma_{\text{ext}} \rangle_{\text{BC}}\cdot\langle \varpi \rangle_{\text{BC}} + \langle \sigma_{\text{ext}} \rangle_{\text{S}}\cdot\langle \varpi \rangle_{\text{S}}}{\langle \sigma_{\text{ext}} \rangle_{\text{EMM}}}, \tag{10}$$

$$\langle g \rangle_{\text{EMM}} = \frac{\langle g \rangle_{\text{BC}}\cdot\langle \sigma_{\text{ext}} \rangle_{\text{BC}}\cdot\langle \varpi \rangle_{\text{BC}} + \langle g \rangle_{\text{S}}\cdot\langle \sigma_{\text{ext}} \rangle_{\text{S}}\cdot\langle \varpi \rangle_{\text{S}}}{\langle \sigma_{\text{ext}} \rangle_{\text{BC}}\cdot\langle \varpi \rangle_{\text{BC}} + \langle \sigma_{\text{ext}} \rangle_{\text{S}}\cdot\langle \varpi \rangle_{\text{S}}}, \tag{11}$$

where the subscript "BC" represents bare BC and the subscript "S" represents sulfate or wet sulfate droplets. The simulation of external OC is obtained simply by replacing the optical properties of sulfate with those of OC.

2.3. RF

To understand the impact of the BC aggregate structure on RF during the hygroscopic growth of aged/mixed BC, we defined aerosol direct RF as

$$\Delta F = F_{\text{aero}} - F_{\text{non-aero}}, \tag{12}$$

where ΔF is the net flux and the subscripts "aero" and "non-aero" represent the conditions with and without aerosol, respectively. ΔF can be approximated both at the TOA and the SFC. The RF for the entire ATMOS is the difference between the RFs at the TOA and SFC. The RF at $RH = a$ caused by hygroscopic growth, $\Delta F_{HG=a}$ is defined as

$$\Delta F_{HG=a} = \Delta F_{RH=a} - \Delta F_{RH=0}, \tag{13}$$

where $\Delta F_{RH=a}$ and $\Delta F_{RH=0}$ are the RFs at RH = a and $RH = 0$, respectively. Meanwhile, $\Delta F_{HG=a}$ can be applied to different mixing conditions (i.e., CAM, CSM, and EMM), so the RF due to internal mixing, ΔF_{MIX}, can be defined as

$$\Delta F_{\text{MIX}} = \Delta F_{\text{IN}} - \Delta F_{\text{EX}}, \tag{14}$$

where ΔF_{IN} and ΔF_{EX} are the RFs of the internally mixed (either CAM or CSM) and externally mixed aerosols, respectively. Clearly, ΔF_{MIX} can be estimated at any RH for either the CAM or CSM case. Again, this study focuses on the RF due to hygroscopic growth or internal mixing, not the forcing due to BC aerosol itself, and the following results should be carefully interpreted. The Santa Barbara DISORT Atmospheric Radiative Transfer model is used (Ricchiazzi et al., 1998) in this study. Our Santa Barbara DISORT Atmospheric Radiative Transfer simulations are validated using an independent RT implementation, that is, the libRadtran (Emde et al., 2016; Mayer & Kylling, 2005), and the two methods give similar results. We verify that the vertical distribution of BC concentration may also influence the RF amplitude and vertical heating profile (Ding et al., 2005; Tripathi et al., 2007) but has much weaker effects on the relative differences than the BC column loading. As a result, this study assumes that the aerosols are located uniformly at the bottom layer of the atmosphere with heights between 0 and 1 km, which can be interpreted as the aerosol being trapped in the planetary boundary layer.

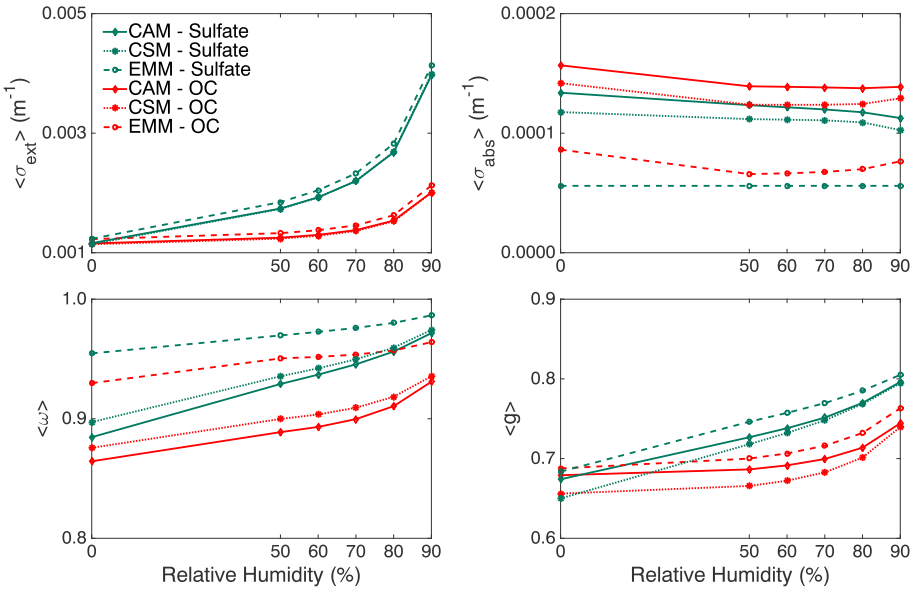

Figure 5. Influence of hygroscopic growth on the bulk optical properties of internally (both coated aggregate and core-shell cases, i.e., CAM and CSM) and externally (EMM) mixed BC particles. OC = organic carbon.

3. Effects on Optical Properties and RF

Figure 5 compares the optical properties, that is, $\langle\sigma_{ext}\rangle$, $\langle\sigma_{abs}\rangle$, $\langle\varpi\rangle$, and $\langle g\rangle$, of aged BC during hygroscopic growth at 550 nm based on the three mixing treatments, that is, the CAM, CSM, and EMM, and we consider both sulfate and OC as the coating materials. The extinction increases significantly with the increase in RH due to hygroscopic growth, especially at larger RH, whereas the absorption shows much less variation over the RH. When the RH reaches 90%, the extinction coefficient is enhanced by ~2–3.5 times compared to the dry case depending on the coating material. Because sulfate is more hydrophilic than OC, the sulfate coating results in a much larger extinction. The increases in the extinction are completely contributed by increases in the scattering because the particles are significantly enlarged by absorbing water (i.e., Figure 3). Unexpectedly, the EMM results in a slightly larger extinction than the corresponding CAM and CSM cases because the BC fraction is small and the extinction of bare sulfate/OC here is almost the same as that with a BC core. The internal mixing cases result in much stronger absorption than the external cases. However, further hygroscopic growth no longer enhances the absorption because the absorption has already increased to almost the maximum due to large sulfate/OC coatings. The CAM results in absorption that is approximately 10% larger than that of the CSM, which agrees with the values shown by Kahnert et al. (2012) and L. Liu and Mishchenko (2018). Although hygroscopic growth enlarges the coating, it also leads to a smaller refractive index, which limits further increases in the absorption. With the variations in $\langle\sigma_{ext}\rangle$ and $\langle\sigma_{abs}\rangle$ discussed, the changes in $\langle\varpi\rangle$ can be easily understood, and $\langle\varpi\rangle$ increases with RH to over 0.9. Even with BC, large $\langle\varpi\rangle$ values are obtained because of the large sulfate/OC volume fraction used in the modeling. The differences in $\langle\varpi\rangle$ among the three mixing structures are relatively significant compared to those of other optical properties, and the differences in the two mixed BC cases decrease due to the hygroscopic growth. The increase in $\langle g\rangle$ (by ~10%) indicates an enhancement of the energy fraction scattered to the forward directions because all particles become larger during hygroscopic growth. The differences in the optical properties between the CAM and CSM decrease as RH increases because the effects of the BC aggregate structure become weaker as the fraction of the coating sphere increases.

Another important factor that has seldom been discussed is the BC core placement with respect to the coating center, and in reality, BC aggregates may appear at any position within the hosting coating. This study fixes the aggregates at the center of the coating sphere, whereas they can also be in an off-center position, partially coated, or attached. Thus, the effects of the BC core placement with respect to the coating center on the optical properties are briefly illustrated in Figure 6. We consider BC aggregates with 200 monomers with five different placements of the BC core with respect to the center of the coated particle, and the five

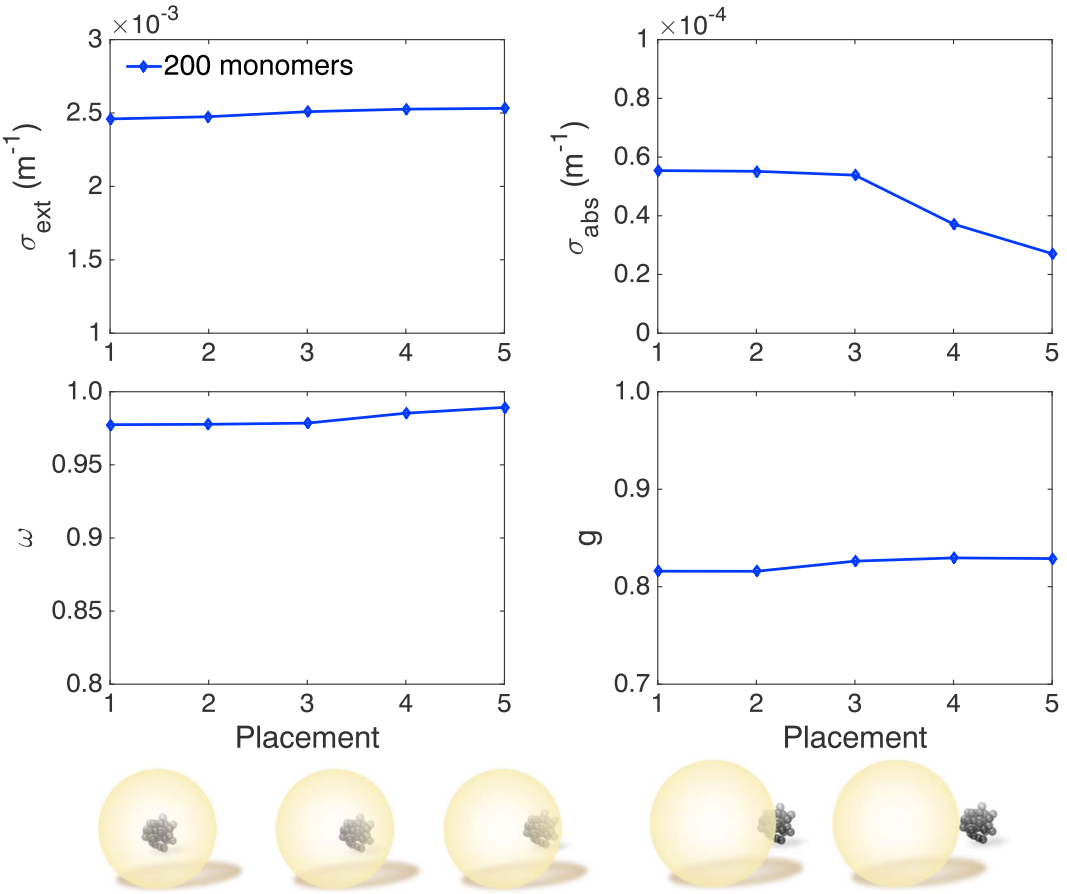

Figure 6. Effects of the black carbon core placement with respect to the coating center on optical properties of coated aggregates. Here we show the case where relative humidity = 90% as an example.

cases are illustrated at the bottom of the figure. An extreme case at RH = 90% is considered to have a sufficiently large enough sulfate sphere for aggregates to move around. As the BC aggregate moves to the edge of the coating sphere, the extinction, single-scattering albedo, and asymmetry factor slightly increase but mostly by less than 2%. However, the absorption shows the most dramatic changes and decreases by over 40% as the BC moves from the inside edge (case 3) to the outside (case 5). This result indicates that BC aggregates entirely inside the coating sphere are optically similar and that the partially coated or attached cases may have optical and radiative properties similar to those of external mixing due to less absorption. With the departure of the BC component from the coating particle, the CAM may result in smaller absorption than the CSM, as shown by Adachi et al. (2010). However, without quantitative knowledge about the realistic positions of the BC and its coating, this study assumes the BC to be completely inside, whereas more detailed research should be carried out to investigate the effects of partial coating in future studies.

Figure 7 illustrates the bulk optical properties of BC internally and externally mixed with sulfate in the solar spectrum in the dry case ($RH = 0$) and after hygroscopic growth at $RH = 90\%$. All optical properties decrease with wavelength because of the decrease in relative size to incident wavelength. The extinctions of internally and externally mixed aerosols are almost indistinguishable. The differences in the absorption are mainly caused by the differences between the internal and external mixing, and the CSM and CAM give much larger absorption results than the external case due to the lensing effects of internal mixing. Because this study considers the scenario that BC particles have been heavily coated under dry conditions (Schnaiter et al., 2005), the wet case does not necessarily further enhance the absorption. The differences between the CAM and CSM may also vary slightly at different wavelengths. The EMM results in a larger single-scattering albedo

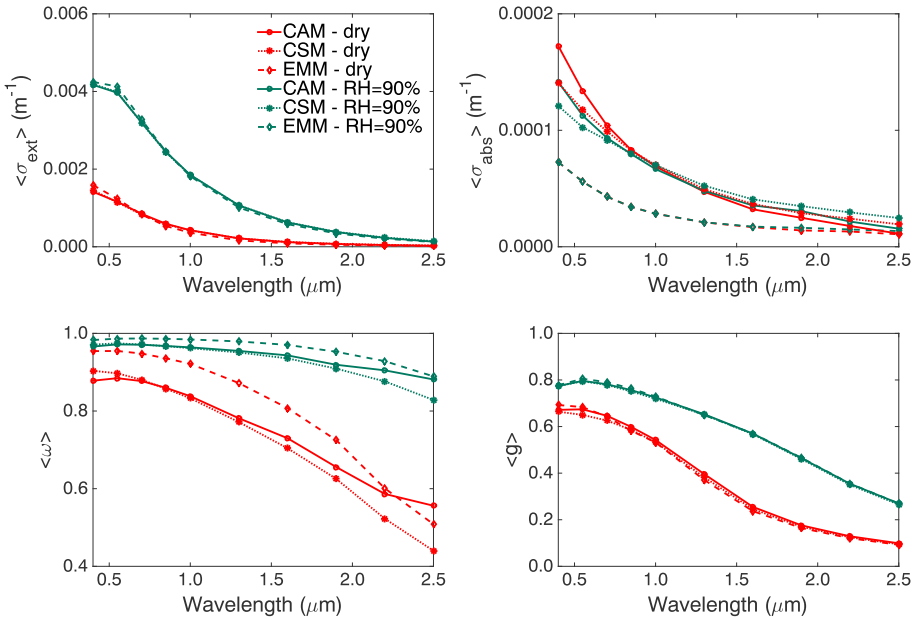

Figure 7. Bulk optical properties of coated aggregate (CAM), core-shell (CSM), and external mixing (EMM) before and after hygroscopic growth at $RH = 90\%$. RH = relative humidity.

than the CAM and CSM, and the asymmetry factors given by the three mixing geometries also closely agree. Most of the differences for the dry and wet cases at different wavelengths are similar to the results shown in Figure 5 at 550 nm.

Radiative transfer simulations are then performed to determine the RF during hygroscopic growth due to mixing or aggregate structure. Figure 8 shows the BC RF with the three mixing geometries at different RHs. A climatic atmospheric profile representing midlatitude summer from the model is used for the simulations. The surface albedo is set to 0.15, a typical value for land such as farmland and soils (Henderson-Sellers & Wilson, 1983), and a solar zenith angle of 60° is considered. A BC column aerosol optical depth

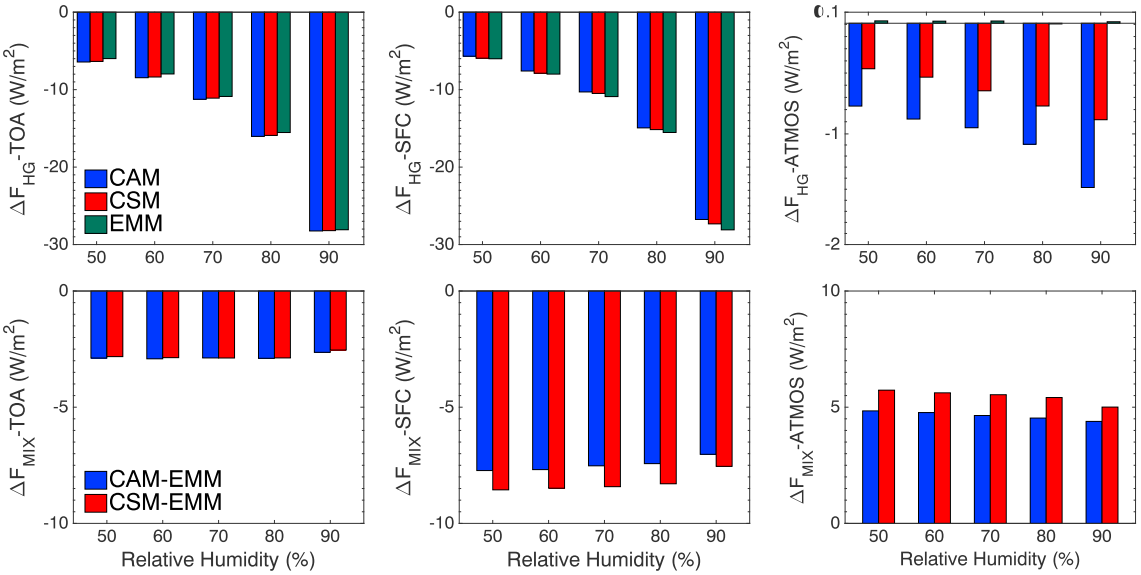

Figure 8. Radiative forcing due to hygroscopic growth (top) and internal mixing (bottom) of aged black carbon coated with sulfate. The optical depth of the bare black carbon at 550 nm is set at 0.01, and the three panels from left to right are for forcing at the TOA, SFC, and ATMOS. TOA = top of the atmosphere; SFC = surface; ATMOS = atmosphere.

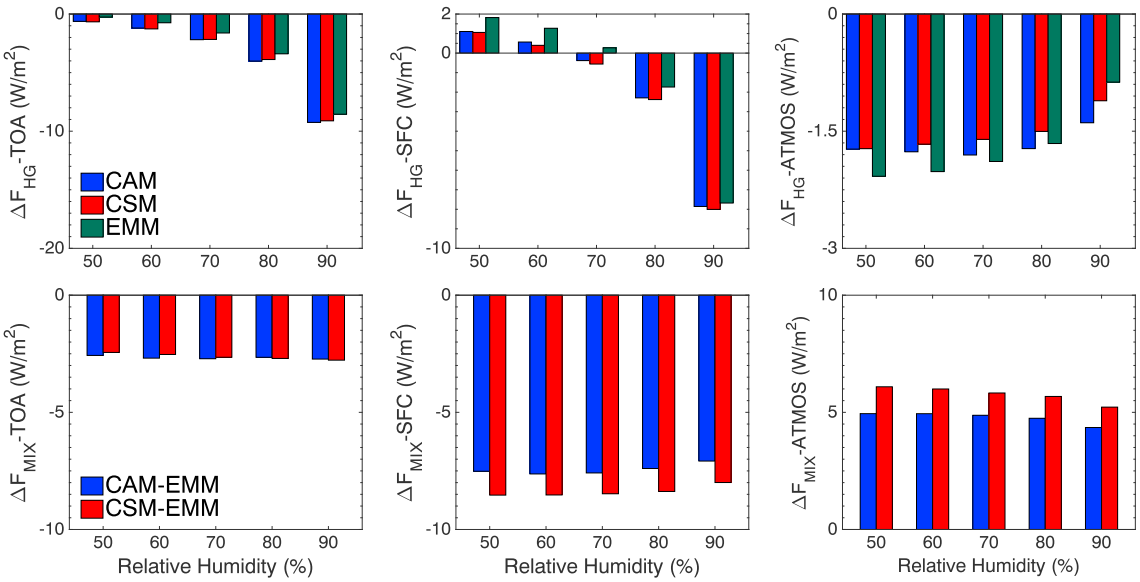

Figure 9. Same as Figure 8 but for aged black carbon coated with organic carbon.

(AOD) of 0.01 (close to the global average mean) before mixing and growth is used to give the BC amount in the layer (Chung, Ramanathan, et al., 2012). Figure 8 illustrates the results for aged BC with sulfate coating. The top panels of Figure 8 show the ΔF_{HG} of mixed BC with the three mixing geometries, that is, CAM, CSM, and EMM. Due to the increased fraction of non-BC materials (and consequent scattering), especially at high RH, the ΔF_{HG} values at the TOA and SFC are negative, and their magnitudes increase with increasing RH. Meanwhile, the forcing in the ATMOS is also slightly negative because it decreases the absorption, as shown in Figure 5. The results for ΔF_{HG} indicates that the hygroscopic growth cools the atmosphere and dims the surface; that is, hygroscopic growth plays a role similar to that of the scattering aerosols. The three mixing conditions give almost the same forcing at the TOA and SFC with relative differences of ~ 5%. The relative differences due to different mixing geometries are more significant for the forcing of the ATMOS, but the absolute values are a few tenths of 1 W/m^2. The EMM results in almost no forcing in the ATMOS because the absorption is unchanged during hygroscopic growth. Compared with the more realistic CAM case, the CSM case may underestimate the RFs in the ATMOS by 40%. The bottom panels of Figure 8 show ΔF_{MIX}, that is, forcing of internal mixing at different RHs. All ΔF_{MIX} at the TOA are negative and less sensitive to the RHs, and the differences between the CAM and CSM are negligible. Compared with the CSM, the CAM results in a smaller magnitude of negative forcing at the SFC and positive forcing in the ATMOS, and both differences are approximately 10%. This result means that by accounting for the effects of the BC aggregate structure, the RFs at the SFC and ATMOS are slightly redistributed, whereas less influence is shown at the TOA. Comparing the top and bottom panels, the forcing caused by hygroscopic growth is stronger at the SFC under high RH conditions and is much weaker in the ATMOS, and their relative effects at the SFC depend on the RH. Overall, for the heavily mixed BC considered in this study, the CSM can give accurate RF at the TOA but introduces slight differences in the forcing of the SFC and ATMOS.

Figure 9 is the same as Figure 8 but for OC-coated particles, and some interesting differences are observed between Figures 8 and 9. OC is weakly absorbing and is much less hydrophilic than sulfate. First, the magnitude of hygroscopic forcing ΔF_{HG} decreases because OC absorbs less water than sulfate. Meanwhile, the forcing at the surface may become slightly positive at low RH, which can be explained by the decrease in absorption of OC at small RH. Additionally, the hygroscopic growth RF in the ATMOS of the EMM results becomes nonzero due to the change in pure OC absorption. For the RFs of internal mixing ΔF_{MIX}, the OC-coated results are the same as those for sulfate. Although a BC AOD of only 0.01 is considered, relatively large RF values are obtained in both Figures 8 and 9. These values are in a range similar to those from previous studies for aerosol RF values in polluted areas (Srivastava & Ramachandran, 2013; Vuolo et al., 2014). This result occurs because the total aerosol AOD may become almost 0.4 after being heavily coated and

hygroscopic growth (as the BC volume fraction is only ~5%), and this value corresponds to some highly polluted regions over land that may have RF near or even larger than -30 W/m^2 at the TOA (García et al., 2012; Vuolo et al., 2014). However, for the simulations, we assume all BC to be heavily coated and to completely grow in the atmosphere which may overestimate the forcing to some degree. In a more realistic scenario, BC may be less coated, and the RF due to hygroscopic growth may be smaller.

4. Conclusions

This study explores the impact of the aggregate structure on BC optical properties and direct RF. The representation of BC particles in optical simulations can be improved by treating them as more realistic nonspherical aggregates. We assume a particle-resolved coating case based on a previous laboratory measurement to reveal the effects of BC aggregates. A series of numerical methods, including the fractal aggregate geometry, κ-Köhler condensation theory, EMT, and MSMT, is used to account for the changes in the microphysical and optical properties of aged BC. To quantify the direct RF due to hygroscopic growth of aged BC, we calculate the optical properties of BC mixtures in different forms, for example, CAM, CSM, and EMM, over the entire solar spectrum. During the aging process, $\langle\sigma_{\text{ext}}\rangle$, $\langle\varpi\rangle$, and $\langle g\rangle$ are altered significantly by an increase in RH. With the heavy coating considered in this study, hygroscopic growth clearly enhances scattering but exerts little effect on absorption. $\langle g\rangle$ increases due to an increase in particle size during hygroscopic growth. Compared with the case considering BC as more realistic aggregates (i.e., the CAM), the CSM slightly underestimates the absorption at visible wavelengths, whereas it shows smaller differences for other optical properties. In terms of RF, hygroscopic growth of internally mixed BC plays a role similar to that of scattering aerosols and can offset the positive RF of BC at the TOA. The CSM gives approximations of the RF at the TOA similar to those of the CAM, whereas the CSM underestimates the radiative effects of hygroscopic growth in the ATMOS by up to 40% (for sulfate coating) and overestimates the radiative effects of internal mixing at the SFC and ATMOS by ~10%. Note that after the hygroscopic growth, BC only accounts for a small fraction in total particle mass/volume, so the implications of our study can also be extended to another regime where particle can serve as cloud condensation nuclei for cloud formation. Also, considering the significant uncertainties in mixing geometries, BC size-fraction relationship, and vertical distributions, the real differences stemming from different BC aggregate assumptions are still debatable, at least not significant for the heavy coating cases.

Acknowledgments
We particularly thank D. M. Mackowski and M. I. Mishchenko for the MSTM code (http://eng.auburn.edu/users/dmckwski/scatcodes/), and Paul Ricchiazzi for the SBDART code (https://www.paulschou.com/tools/sbdart/). All data related to this work are available online (https://github.com/Zeng86/Hygroscopic-growth-data). This work was financially supported by the National Key Research and Development Program of China (2016YFA0602003), the National Natural Science Foundation of China (NSFC) grants 41571348 and 41590873, and the Young Elite Scientists Sponsorship Program by CAST (2017NRC001).

References

Ackermann, I. J., Hass, H., Memmesheimer, M., Ebel, A., Binkowski, F. S., & Shankar, U. M. A. (1998). Modal aerosol dynamics model for Europe: Development and first applications. *Atmospheric Environment*, *32*(17), 2981–2999. https://doi.org/10.1016/S1352-2310(98)00006-5

Adachi, K., Chung, S. H., & Buseck, P. R. (2010). Shapes of soot aerosol particles and implications for their effects on climate. *Journal of Geophysical Research*, *115*, D15206. https://doi.org/10.1029/2009JD012868

Adams, P. J., & Seinfeld, J. H. (2002). Predicting global aerosol size distributions in general circulation models. *Journal of Geophysical Research*, *107*(D19), 4370. https://doi.org/10.1029/2001JD001010

Adler, G., Riziq, A. A., Erlick, C., & Rudich, Y. (2010). Effect of intrinsic organic carbon on the optical properties of fresh diesel soot. *Proceedings of the National Academy of Sciences of the United States of America*, *107*, 6690–6704.

Aquila, V., Hendricks, J., Lauer, A., Riemer, N., Vogel, H., Baumgardner, D., et al. (2011). MADE-in: A new aerosol microphysics submodel for global simulation of insoluble particles and their mixing state. *Geoscientific Model Development*, *4*(2), 325–355. https://doi.org/10.5194/gmd-4-325-2011

Bond, T. C., Doherty, S. J., Fahey, D. W., Forster, P. M., Berntsen, T., DeAngelo, B. J., et al. (2013). Bounding the role of black carbon in the climate system: A scientific assessment. *Journal of Geophysical Research: Atmospheres*, *118*, 380–552. https://doi.org/10.1002/jgrd.50171

Cappa, C. D., Onasch, T. B., Massoli, P., Worsnop, D. R., Bates, T. S., Cross, E. S., et al. (2012). Radiative absorption enhancements due to the mixing state of atmospheric black carbon. *Science*, *337*(6098), 1078–1081. https://doi.org/10.1126/science.1223447

Chakrabarty, R. K., Moosmüller, H., Garro, M. A., Arnott, W. P., Walker, J., Susott, R. A., et al. (2006). Emissions from the laboratory combustion of wild land fuels: Particle morphology and size. *Journal of Geophysical Research*, *111*, D07204. https://doi.org/10.1029/2005JD006659

Chang, R. W., Slowik, J. G., Shantz, N. C., Vlasenko, A., Liggio, J., Sjostedt, S. J., et al. (2010). The hygroscopicity parameter of ambient organic aerosol at a field site subject to biogenic and anthropogenic influences: Relationship to degree of aerosol oxidation. *Atmospheric Chemistry and Physics*, *10*, 47–64.

Chin, M., Rood, R. B., Lin, S. J., Müller, J. F., & Thompson, A. M. (2000). Atmospheric sulfur cycle simulated in the global model GOCART: Model description and global properties. *Journal of Geophysical Research*, *105*(D20), 24,671–24,687. https://doi.org/10.1029/2000JD900384

Ching, J., Zaveri, R. A., Easter, R. C., Riemer, N., & Fast, J. D. (2016). A three-dimensional sectional representation of aerosol mixing state for simulating optical properties and cloud condensation nuclei. *Journal of Geophysical Research: Atmospheres*, *121*, 5912–5929. https://doi.org/10.1002/2015JD024323

Chung, C. E., Lee, K., & Mueller, D. (2012). Effect of internal mixture on black carbon radiative forcing. *Tellus Series B: Chemical and Physical Meteorology*, *64*(1). https://doi.org/10.3402/tellusb.v64i0.10925

Chung, C. E., Ramanathan, V., & Decremer, D. (2012). Observationally constrained estimates of carbonaceous aerosol radiative forcing. *Proceedings of the National Academy of Sciences of the United States of America*, *109*(29), 11,624–11,629. https://doi.org/10.1073/pnas.1203707109

Chýlek, P., Videen, G., Geldart, D. J., Dobbie, J. S., & Tso, H. C. (2000). Effective medium approximations for heterogeneous particles. In M. I. Mishchenko, J. W. Hovenier, & L. D. Travis (Eds.), *Light scattering by nonspherical particles*, (pp. 273–308). San Diego: Academic Press. https://doi.org/10.1016/B978-012498660-2/50036-7

Cruz, N. C., & Pandis, S. N. (2000). Deliquescence and hygroscopic growth of mixed inorganic-organic atmospheric aerosol. *Environmental Science & Technology*, *34*(20), 4313–4319. https://doi.org/10.1021/es9907109

D'Almeida, G. A., Koepke, P., & Shettle, E. P. (1991). *Atmospheric aerosols: Global climatology and radiative characteristics*. Hampton, VA: A Deepak Publishing.

Ding, G. A., Chan, C., Gao, Z., Yao, W., Li, Y., Cheng, X., et al. (2005). Vertical structures of PM10 and PM2. 5 and their dynamical character in low atmosphere in Beijing urban areas. *Science China*, *48*, 38–54.

Emde, C., Buras-Schnell, R., Kylling, A., Mayer, B., Gasteiger, J., Hamann, U., et al. (2016). The libRadtran software package for radiative transfer calculations (version 2.0.1). *Geoscientific Model Development*, *9*(5), 1647–1672. https://doi.org/10.5194/gmd-9-1647-2016

Fierce, L., Bond, T. C., Bauer, S. E., Mena, F., & Riemer, N. (2016). Black carbon absorption at the global scale is affected by particle-scale diversity in composition. *Nature Communications*, *7*(1). https://doi.org/10.1038/ncomms12361

Fierce, L., Riemer, N., & Bond, T. C. (2017). Toward reduced representation of mixing state for simulating aerosol effects on climate. *Bulletin of The American Meteorological Society*, *98*(5), 971–980. https://doi.org/10.1175/BAMS-D-16-0028.1

Filippov, A. V., Zurita, M., & Rosner, D. E. (2000). Fractal-like aggregates: Relation between morphology and physical properties. *Journal of Colloid and Interface Science*, *229*(1), 261–273. https://doi.org/10.1006/jcis.2000.7027

García, O. E., Díaz, J. P., Expósito, F. J., Díaz, A. M., Dubovik, O., Dubuisson, P., & Roger, J. C. (2012). Shortwave radiative forcing and efficiency of key aerosol types using AERONET data. *Atmospheric Chemistry and Physics*, *12*(11), 5129–5145. https://doi.org/10.5194/acp-12-5129-2012

Hale, G., & Querry, M. (1984). Optical constants of water in the 200 nm to 200 mm wavelength region. *Applied Optics*, *23*, 1206–1225.

Hämeri, K., Väkevä, M., Hansson, H. C., & Laaksonen, A. (2000). Hygroscopic growth of ultrafine ammonium sulphate aerosol measured using an ultrafine tandem differential mobility analyzer. *Journal of Geophysical Research*, *105*(D17), 22,231–22,242. https://doi.org/10.1029/2000JD900220

Hansen, J., Sato, M., & Ruedy, R. (1997). Radiative forcing and climate response. *Journal of Geophysical Research*, *102*(D6), 6831–6864. https://doi.org/10.1029/96JD03436

He, C., Li, Q., Liou, K. N., Qi, L., Tao, S., & Schwarz, J. P. (2016). Microphysics-based black carbon aging in a global CTM: Constraints from HIPPO observations and implications for global black carbon budget. *Atmospheric Chemistry and Physics*, *16*(5), 3077–3098. https://doi.org/10.5194/acp-16-3077-2016

He, C., Liou, K. N., Takano, Y., Zhang, R., Levy Zamora, M., Yang, P., et al. (2015). Variation of the radiative properties during black carbon aging: Theoretical and experimental intercomparison. *Atmospheric Chemistry and Physics*, *15*(20), 11,967–11,980. https://doi.org/10.5194/acp-15-11967-2015

Henderson-Sellers, A., & Wilson, M. F. (1983). Surface albedo data for climatic modeling. *Reviews of Geophysics*, *21*(8), 1743–1778. https://doi.org/10.1029/RG021i008p01743

Jacobson, M. Z. (2001). Strong radiative heating due to the mixing state of black carbon in atmospheric aerosols. *Nature*, *409*(6821), 695–697. https://doi.org/10.1038/35055518

Kahnert, M., & Devasthale, A. (2011). Black carbon fractal morphology and short-wave radiative impact: A modelling study. *Atmospheric Chemistry and Physics*, *11*(22), 11,745–11,759. https://doi.org/10.5194/acp-11-11745-2011

Kahnert, M., Nousiainen, T., Lindqvist, H., & Ebert, M. (2012). Optical properties of light absorbing carbon aggregates mixed with sulfate: Assessment of different model geometries for climate forcing calculations. *Optics Express*, *20*(9), 10042–10058. https://doi.org/10.1364/OE.20.010042

Lee, Y. H., & Adams, P. J. (2010). Evaluation of aerosol distributions in the GISS-TOMAS global aerosol microphysics model with remote sensing observations. *Atmospheric Chemistry and Physics*, *10*(5), 2129–2144. https://doi.org/10.5194/acp-10-2129-2010

Lesins, G., Chýlek, P., & Lohmann, U. (2002). A study of internal and external mixing scenarios and its effect on aerosol optical properties and direct radiative forcing. *Journal of Geophysical Research*, *107*(D10), 4094. https://doi.org/10.1029/2001JD000973

Li, J., Liu, C., Yin, Y., & Kumar, K. R. (2016). Numerical investigation on the Ångström exponent of black carbon aerosol. *Journal of Geophysical Research: Atmospheres*, *121*, 3506–3518. https://doi.org/10.1002/2015JD024718

Li, K., Liao, H., Mao, Y., & Ridley, D. A. (2016). Source sector and region contributions to concentration and direct radiative forcing of black carbon in China. *Atmospheric Environment*, *124*, 351–366. https://doi.org/10.1016/j.atmosenv.2015.06.014

Liu, C., Chul, C. E., Yin, Y., & Schnaiter, M. (2018). The absorption Ångström exponent of black carbon: From numerical aspects. *Atmospheric Chemistry and Physics*, *18*(9), 6259–6273. https://doi.org/10.5194/acp-18-6259-2018

Liu, C., Li, J., Yin, Y., Zhu, B., & Feng, Q. (2017). Optical properties of black carbon aggregates with non-absorptive coating. *Journal of Quantitative Spectroscopy & Radiative Transfer*, *187*, 443–452. https://doi.org/10.1016/j.jqsrt.2016.10.023

Liu, C., Panetta, R. L., & Yang, P. (2014). Inhomogeneity structure and the applicability of effective medium approximations in calculating light scattering by inhomogeneous particles. *Journal of Quantitative Spectroscopy & Radiative Transfer*, *146*, 331–348. https://doi.org/10.1016/j.jqsrt.2014.03.018

Liu, D., Allan, J., Whitehead, J., Young, D., Flynn, M., Coe, H., et al. (2013). Ambient black carbon particle hygroscopic properties controlled by mixing state and composition. *Atmospheric Chemistry and Physics*, *13*(4), 2015–2029. https://doi.org/10.5194/acp-13-2015-2013

Liu, H., Zhao, C., Nekat, B., Ma, N., Wiedensohler, A., Van Pinxteren, D., et al. (2014). Aerosol hygroscopicity derived from size-segregated chemical composition and its parameterization in the North China Plain. *Atmospheric Chemistry and Physics*, *14*(5), 2525–2539. https://doi.org/10.5194/acp-14-2525-2014

Liu, L., & Mishchenko, M. (2018). Scattering and radiative properties of morphologically complex carbonaceous aerosols: A systematic modeling study. *Remote Sensing*, *10*(10). https://doi.org/10.3390/rs10101634

Liu, S., Aiken, A. C., Gorkowski, K., Dubey, M. K., Cappa, C. D., Williams, L. R., et al. (2015). Enhanced light absorption by mixed source black and brown carbon particles in UK winter. *Nature Communications*, *8435*. https://doi.org/10.1038/ncommms9435

Mackowski, D. W., & Mishchenko, M. I. (2011). A multiple sphere T-matrix Fortran code for use on parallel computer clusters. *Journal of Quantitative Spectroscopy & Radiative Transfer*, *112*(13), 2182–2192. https://doi.org/10.1016/j.jqsrt.2011.02.019

Matsui, H., Hamilton, D. S., & Mahowald, N. M. (2018). Black carbon radiative effects highly sensitive to emitted particle size when resolving mixing-state diversity. *Nature Communications*, *9*(1), 3446. https://doi.org/10.1038/s41467-018-05635-1

Matsui, H., Koike, M., Kondo, Y., Moteki, N., Fast, J. D., & Zaveri, R. A. (2013). Development and validation of a black carbon mixing state resolved three-dimensional model: Aging processes and radiative impact. *Journal of Geophysical Research: Atmospheres*, *118*, 2304–2326. https://doi.org/10.1029/2012JD018446

Mayer, B., & Kylling, A. (2005). The libRadtran software package for radiative transfer calculations-description and examples of use. *Atmospheric Chemistry and Physics*, *5*(7), 1855–1877. https://doi.org/10.5194/acp-5-1855-2005

Menon, S., Hansen, J., Nazarenko, L., & Luo, Y. (2002). Climate effects of black carbon aerosols in China and India. *Science*, *297*(5590), 2250–2253. https://doi.org/10.1126/science.1075159

Myhre, G., Samset, B. H., Schulz, M., Balkanski, Y., Bauer, S., Berntsen, T. K., et al. (2013). Radiative forcing of the direct aerosol effect from AeroCom Phase II simulations. *Atmospheric Chemistry and Physics*, *13*(4), 1853–1877. https://doi.org/10.5194/acp-13-1853-2013

Peng, J., Hu, M., Guo, S., Du, Z., Zheng, J., Shang, D., et al. (2016). Markedly enhanced absorption and direct radiative forcing of black carbon under polluted urban environments. *Proceedings of the National Academy of Sciences of the United States of America*, *113*(16), 4266–4271. https://doi.org/10.1073/pnas.1602310113

Ramanathan, V., & Carmichael, G. (2008). Global and regional climate changes due to black carbon. *Nature Geoscience*, *1*(4), 221–227. https://doi.org/10.1038/ngeo156

Ricchiazzi, P., Yang, S., Gautier, C., & Sowle, D. (1998). SBDART: A research and teaching software tool for plane-parallel radiative transfer in the Earth's atmosphere. *Bulletin of The American Meteorological Society Impact*, *79*(10), 2101–2114. https://doi.org/10.1175/1520-0477(1998)079<2101:SARATS>2.0.CO;2

Riemer, N., West, M., Zaveri, R., & Easter, R. (2010). Estimating black carbon aging time-scales with a particle-resolved aerosol model. *Journal of Aerosol Science*, *41*(1), 143–158. https://doi.org/10.1016/j.jaerosci.2009.08.009

Riemer, N., West, M., Zaveri, R. A., & Easter, R. C. (2009). Simulating the evolution of soot mixing state with a particle-resolved aerosol model. *Journal of Geophysical Research*, *114*, D09202. https://doi.org/10.1029/2008JD011073

Schnaiter, M., Linke, C., Möhler, O., Naumann, K. H., Saathoff, H., Wagner, R., et al. (2005). Absorption amplification of black carbon internally mixed with secondary organic aerosol. *Journal of Geophysical Research*, *110*, D19204. https://doi.org/10.1029/2005JD006046

Smith, A. J. A., & Grainger, R. G. (2014). Simplifying the calculation of light scattering properties for black carbon fractal aggregates. *Atmospheric Chemistry and Physics*, *14*(15), 7825–7836. https://doi.org/10.5194/acp-14-7825-2014

Sorensen, C. M. (2001). Light scattering by fractal aggregates: A review. *Aerosol Science and Technology*, *35*(2), 648–687. https://doi.org/10.1080/02786820117868

Srivastava, R., & Ramachandran, S. (2013). The mixing state of aerosols over the Indo-Gangetic Plain and its impact on radiative forcing. *Quarterly Journal of the Royal Meteorological Society*, *139*(670), 137–151. https://doi.org/10.1002/qj.1958

Toon, O. B., Pollack, J. B., & Khare, B. N. (1976). The optical constants of several atmospheric aerosol species: Ammonium sulfate, ammonium oxide and sodium chloride. *Journal of Geophysical Research*, *81*(33), 5733–5748. https://doi.org/10.1029/JC081i033p05733

Tripathi, S. N., Srivastava, A. K., Dey, S., Satheesh, S. K., & Krishnamoorthy, K. (2007). The vertical profile of atmospheric heating rate of black carbon aerosols at Kanpur in northern India. *Atmospheric Environment*, *41*(32), 6909–6915. https://doi.org/10.1016/j.atmosenv.2007.06.032

Vuolo, M. R., Schulz, M., Balkanski, Y., & Takemura, T. (2014). A new method for evaluating the impact of vertical distribution on aerosol radiative forcing in general circulation models. *Atmospheric Chemistry and Physics*, *14*(2), 877–897. https://doi.org/10.5194/acp-14-877-2014

Wang, Y., Jiang, J. H., & Su, H. (2015). Atmospheric responses to the redistribution of anthropogenic aerosols. *Journal of Geophysical Research: Atmospheres*, *120*, 9625–9641. https://doi.org/10.1002/2015JD023665

Wang, Y., Khalizov, A., Levy, M., & Zhang, R. (2013). New directions: Light absorbing aerosols and their atmospheric impacts. *Atmospheric Environment*, *81*, 713–715. https://doi.org/10.1016/j.atmosenv.2013.09.034

Wang, Y., Liu, F., He, C., Bi, L., Cheng, T., Wang, Z., et al. (2017). Fractal dimensions and mixing structures of soot particles during atmospheric processing. *Environmental Science & Technology Letters*, *4*(11), 487–493. https://doi.org/10.1021/acs.estlett.7b00418

Wang, Y., Ma, P.-L., Peng, J., Zhang, R., Jiang, J. H., Easter, R. C., & Yung, Y. L. (2018). Constraining aging processes of black carbon in the Community Atmosphere Model using environmental chamber measurements. *Journal of Advances in Modeling Earth Systems*, *10*, 2514–2526. https://doi.org/10.1029/2018MS001387

Weingartner, E., Burtscher, H., & Baltensperger, U. (1997). Hygroscopic properties of carbon and diesel soot particles. *Atmospheric Environment*, *31*(15), 2311–2327. https://doi.org/10.1016/S1352-2310(97)00023-X

Zaveri, R. A., Barnard, J. C., Easter, R. C., Riemer, N., & West, M. (2010). Particle-resolved simulation of aerosol size, composition, mixing state, and the associated optical and cloud condensation nuclei activation properties in an evolving urban plume. *Journal of Geophysical Research*, *115*, D17210. https://doi.org/10.1029/2009JD013616

Zaveri, R. A., Easter, R. C., Fast, J. D., & Peters, L. K. (2008). Model for simulating aerosol interactions and chemistry (MOSAIC). *Journal of Geophysical Research*, *113*, D13204. https://doi.org/10.1029/2007JD008782